

Explosive Disruption of Polytropes: a One Dimensional Hydrodynamic Calculation

Mark Wyman^{1,2}, David Chernoff¹, and Ira Wasserman^{1,2}

¹ *Center for Radiophysics and Space Research, Cornell University, Ithaca, NY 14853, USA*

² *Laboratory for Elementary Particle Physics, Cornell University, Ithaca, NY 14853, USA*

mark.wyman@cornell.edu, chernoff@astro.cornell.edu, ira@astro.cornell.edu

ABSTRACT

We study explosions of stars using a one-dimensional Lagrangian hydrodynamics code. We calculate how much mass is liberated as a function of the energy of explosion for a variety of pre-explosion stellar structures and for equations of state with a range of radiation-to-gas pressure ratios. The results show that simple assumptions about the amount of mass lost in an explosion can be quite inaccurate, and that even one-dimensional stars exhibit a rich phenomenology. The mass loss fraction rises from about 50 to 100% as a function of the explosion energy in an approximately discontinuous manner. We suggest that Nova Scorpii (J1655-40) may have experienced significant mass fallback because the explosion energy was less than the critical value. We infer that the original progenitor was less than twice the mass of today's remnant.

Subject headings: supernovae: general, computational; hydrodynamics

1. Introduction

A fundamental question in the study of supernovae is to determine the fate of a star subject to an explosion: is the star disrupted by an explosion of a given strength and, if not, how much of the star is lost and what is the configuration of the matter that remains bound? Many researchers have addressed this question for specific cases of interest using detailed numerical simulation. To our knowledge, a precise description of the relationship between the strength of the explosion and the fate of the outer layers, even in the case of highly idealized stellar models, has never been given. The potential utility of this information is evident in the analysis of Fryer & Kalogera (2001), where an estimate of the amount of mass left bound in the remnant of a supernova, essentially a dimensional estimate, is used to

assess which high mass stars yield neutron stars and which ones yield black holes. The simple “rule of thumb” is that a portion (between 30 and 50%) of the explosion energy is effective in directly unbinding the star; the portion is based on a sparse set of detailed simulations of MacFadyen, Woosley & Heger (1999). Our goal is to improve our understanding of the disruption process by carrying out hydrodynamical calculations of simple stellar models with a range of explosion strengths, a range of stellar structures and a range of equations of state. The results yield improved estimates of the “rule of thumb” which we provide in simple, easily applied, empirical form. A host of significant modeling uncertainties of core collapse (hydrodynamic motions in the core, distribution of angular momentum within the collapsing object, neutrino-matter coupling, etc.) remain, of course, but better answers to the questions we have posed will provide incremental improvement in the determination of the fate of central remnants.

Because the principal focus of this work is explosions that do not completely destroy the star, our simulations involve material that falls back onto the remnant. Our results may also be used to determine the accretion rate of the fallback for the case of simple, idealized stellar structures. There is considerable evidence that a supernova explosion occurred in J1655-40: the atmosphere of its companion is contaminated with elements thought to be formed only in supernovae (Israelian et al. (1999)), and it is likely that the black hole progenitor was considerably more massive than the remnant we see today (Orosz & Bailyn (1997); Shahbaz et al. (1999)). There is also some evidence that the J1655-40 system could have remained bound only if it received a substantial kick during or shortly after the formation of its black hole (Mirabel et al. (2002)). In future papers we intend to explore the connections between the following possibilities: the initial collapse of the core to a neutron star, the impulse the core received (kicked by one of several physical mechanisms thought to be responsible for high pulsar velocities), and the accretion driving the black hole formation. The mass fallback may trigger the collapse to a black hole as well as provide the source of the pollution the companion’s atmosphere. This work begins our investigation of the connections between substantial, as distinct from incremental (*i.e.* several M_{\odot} , not $\sim 0.1M_{\odot}$) fallback, core fate, kick size, and binary survival.

In section 2, we describe the physical set up, while section 3 describes the numerical code. In section 4, we give more detailed results and discuss how the numerical data were analyzed.

2. Problem and Parameter Ranges

We model the supernova as a spherically symmetric explosion in a star that is initially in hydrostatic equilibrium. The pre-explosion stellar structure is a polytrope. We deposit the full energy of the explosion in a small region near the center of star. Using a finite-difference code we calculate the hydrodynamical evolution. A shock propagates towards the surface and the outer layers of the star may be ejected. If the star is not completely destroyed, some of the matter remains gravitationally bound and we follow the evolution long enough to make an accurate estimate of the mass of the bound object.

We considered a range of initial stellar structures. We varied the polytropic index Γ where $P \propto \rho^\Gamma$. The Lane-Emden equation prescribes the run of density and pressure of the initial model; our choices for $n = 1/(\Gamma - 1)$ span $3/2 \leq n \leq 4$. As is well-known, the polytrope’s central to average density ratio increases as n varies from 0 to 5. The range we simulate subsumes typical main-sequence profiles and extended red-giant structures.

We have considered two equation of state treatments: ideal gas pressure (“EOS M”: $P = P_{matter}$ with a fixed ratio of specific heats γ) and a mixture of gas plus radiation in thermal equilibrium (“EOS MR”: $P = P_{rad} + P_{matter}$). EOS M is suitable for stars of low mass (dominated by particle pressure at their centers) and weak explosions (such that the post-shock gas is not radiation dominated); EOS MR is needed if there is significant radiation pressure. We infer the temperature profile from the appropriate EOS and the Lane-Emden pressure-density profile. For low-mass stars, the ratio of radiation-to-gas pressure, $s = P_{rad}/P_{matter}$, at the center of the star depends only on the star’s mass. The central values for $s = s_c$ span $0 \leq s_c < 5.5$, i.e. the stars’ hydrostatic pressure varies from matter-dominated to radiation-dominated (the upper limit was set by the fact that, for $s_c \gtrsim 6$, the inner parts of the star have positive local energy even before the explosion). Of course, the shocks generated by the explosion heat the gas and increase its entropy, and the typical value of radiation-to-gas pressure during the explosion depends not only upon s_c but also upon the energy of the explosion E_{blast} .

We considered a range of explosion energies. Given that we are concerned with analyzing under what circumstances the star is disrupted, we typically considered blasts with $0.1 \leq E_{blast}/E_{bind} \leq 1.5$, i.e. energies of the same order of magnitude as a simple dimensional estimate for unbinding. Readers primarily interested in the results of the calculation are encouraged to skip to §4.

3. The Code and Numerical Tests

3.1. Equations

We use the inviscid fluid equations which describe mass, momentum and energy conservation. All calculations are one-dimensional with either a plane-parallel (for testing) or spherical (for testing and simulations) geometry. We advance the fluid state using a finite difference approximation to the fluid equations (Lax-Wendroff, explicitly differenced, 1-D Lagrangian code (Richtmyer & Morten (1967))). Shocks are handled with the addition of artificial viscosity. We solve Poisson’s equation to determine the gravitational forces of the spherical distribution of matter on each time step. Details are provided in Appendix 1.

3.2. Tests of Hydrodynamics

We tested the purely hydrodynamic capabilities of the code (no gravity) on the Sod shock tube problem (plane-parallel geometry) and on the Sedov blast (spherical geometry). For the Sod test with $\gamma = 7/5$ (as well as for a range of other γ ’s), EOS M, and various overpressures ($p_2/p_1 = 10, 100, 1000$) and 1200 zones, we found essentially perfect agreement of the numerical and analytic solutions except for the shock smearing over $\sim 5 - 8$ zones.

For the Sedov problem, we re-derived the solution given in Landau & Lifschitz’s *Fluid Mechanics* (1987), thereby finding the correction to the often remarked upon error (in an exponent) in that book’s solution. Appendix 2 gives the full solution. We carried out a number of variants of the basic blast wave simulation in terms of EOS and γ . For flows dominated by particle pressure we compared numerical solutions ($\gamma = 5/3$ and $7/5$ for EOS M) with the analytic similarity solution (with γ matched; see Appendix 2). For flows dominated by radiation pressure we compared several different radiation-dominated numerical solutions ($\gamma = 5/3$, EOS MR) to the $\gamma = 4/3$ similarity solution. The radiation-dominated numerical solutions were generated using cold preshock gas so that the explosions yielded a high Mach number flow and $P_{rad}/P_{matter} \gg 1$ in the postshock region. A range of initial s and shock energies was considered. A simulation with large constant $s \sim 1000$ and relatively small explosion and a simulation with small constant $s \sim 0.1$ and large explosion both yield a radiation-dominated numerical solution.

The explosion was allowed to expand to well over 100 times the initial “bomb zone” in all cases. Comparisons of EOS M runs with analytic solutions were possible throughout the simulation; comparisons of EOS MR runs with the analytic radiation-dominated similarity $\gamma = 4/3$ solution was meaningful only for the part of the simulation in which radiation

pressure dominated matter pressure, approximately 4-5 expansion times. With 800 zones, the Sedov test gave close (2 – 3%) agreement in the relative density, velocity and pressure of the numerical solution and the analytic similarity solution for both particle pressure dominated and for radiation pressure dominated flows except in the central-most region.

Two factors contribute to the discrepancies at the center. First, the innermost zone was simply treated as an adiabatic expanding/contracting bubble. The entropy of this zone was incorrect but its mass was so small that its impact on the rest of the solution was inconsequential. The explosion results were found to be almost entirely insensitive to alternative methods of treating this inner zone, provided the treatments were non-singular and energy conserving. Second, explosive energy was injected in a small, but non-negligible central region (typically the inner 5% of the mass). Departures between the analytic solution and the part of the grid used as the “bomb zone” persisted through the simulation, maintained by a persistent contact discontinuity. We also compared two models for the energy injection at the center. For one, the “thermal bomb,” an excess of thermal energy equal to the desired explosion energy was added by hand to the core (inner 5% of the mass) of the star, essentially creating an out-of-equilibrium hot core that then expanded rapidly out into the stellar envelope. In the other, the “kinetic bomb,” a linear velocity profile carrying the same amount of energy was added to the inner 5% of the mass. Both methods produced identical results outside the “bomb zone.”

3.3. Tests of Hydrostatics

With the inclusion of self-gravity forces, we verified that Runge-Kutta integration of the Lane-Emden equations yielded stationary, stable configurations for our time-dependent hydrodynamic evolution equations (finite difference scheme). We verified the long-lived stability for all polytropic indices and radiation-to-gas pressure ratios adopted in this study. Likewise, we verified that the virial theorem was satisfied by the initial configurations.

3.4. Tests of Self-gravitating Explosions

In the actual runs of the problem of interest, we further verified that the treatment of the central zone made no discernible difference, that variations in the “bomb zone” (3-10%, for instance), caused only very slight ($< 5\%$) changes to the amount of mass lost in the explosions. In a Lagrangian code, mass is explicitly conserved. We also verified that energy conservation was satisfied (to $< 5\%$).

4. Results

We adopted polytropes for the initial stellar structure with $P = k\rho^\Gamma$. The density and pressure profile is determined by solution of the Lane-Emden equation with the total mass and radius scaled to unity. We refer to this as the dimensionless solution; it depends only upon Γ . The dimensionless density-pressure distributions are the forms used in our computations. In the results, we discuss dimensionless quantities (explosion energy in terms of binding energy, mass loss in terms of the total mass, etc.) so that our results can be scaled to physical situations as needed.

4.1. Scaling of Polytropes

Let us first review the scaling of the initial polytropic solution. For given k and Γ it is possible to generate a one-parameter family of scaled solutions where M and R vary such that $M \propto R^{(3\Gamma-4)/(\Gamma-2)}$. Or, if one chooses not to regard k as a known quantity, one can specify arbitrary M and R and infer the appropriate value for k .

If one imposes the additional requirement that there be a fixed value of the radiation-to-gas pressure in the initial stellar structure at the center $s = s_c$, the scaling of the dimensionless solution is restricted. For given Γ and k , fixing s_c determines both M and R (no scaling remains); or, if we regard k as an inferred quantity, the choice of s_c permits M to be specified and R is consequently determined. In the limit $s_c \ll 1$, with k undetermined, the full scaling in M and R is recovered.

In this paper we will adopt the point of view that k is not known a priori and we will allow scaling of the polytropic solution to arbitrary M and R in cases with no radiation pressure. In cases with radiation pressure, a scaling relationship between M and R is implied by setting the matter-to-radiation pressure ratio s at one point in the star.

4.2. Description of Analysis

The chief way in which we shall summarize the results of an explosion is in terms of the mass ejected as a function of explosion energy. We begin by discussing how we derive the ejected mass from the numerical simulations. For EOS M (no radiation pressure), the code was run until the remnant core had become stationary and had nearly reassumed hydrostatic equilibrium, i.e., it had local gas velocities near zero ($< 10^{-7} R_{stellar}/\text{dynamical time}$) and satisfied the virial theorem. The mass loss was determined by finding the location in the

outermost Lagrangian grid of the zone for which the local energy (sum of kinetic, thermal and gravitational contributions) density changed from negative to positive. A graph of the local energy density for a typical star after an explosion is included as Fig. 1.

A drawback of this method is apparent in Fig. 1. Though there are distinct portions of the star that can definitely be said to be either remnant or ejecta, there is also a small region with nearly zero energy, resembling an atmosphere around the remnant. These atmospheres did not appear in all explosions – typically, they occurred when $E_{blast} \sim 70\text{--}100\% E_{bind}$ – and when they did, the code was simply run long enough for a reasonably clear separation to be determined. The situation was worst in cases with significant radiation pressure (EOS MR). Such stars had long-period, time-dependent motions. We can understand this tendency as a consequence of the initial conditions (large s_c) or of strong shocks (large explosion energy) that increase the radiation pressure. A simple determination of the radiation-to-matter pressure follows from assuming (1) uniform initial s_0 , (2) explosion energy $\beta = 1 + E_{blast}/E_{bind}$ and (3) uniform post-explosion s_1 gives

$$s_1^{1/3}(1 + 3s_1) = \beta s_0^{1/3}(1 + 3s_0).$$

The size of an explosion that leaves a remnant of any type implies that β is at most a few. So, small s_0 (matter dominated stars) will not give rise to radiation dominated remnants. Such remnants require moderate to large s_0 . In fact, the long-period motions occurred in two cases: for stars with $s_0 = 1$ and $\beta > 2$, and for all stars with $s_0 = 5.5$. The artificial viscosity eventually damps such motions but may take a long time to do so.

In light of this, we moved to a different method for deciding which mass shells were ejecta and which were remnants. We stored the location and local energy density of each grid zone throughout the run time. We plotted the location of the mass element as a function of time, using the sign of the local energy density to color code the lines. During the atmospheric motions some layers do work on other layers; the color coding shows changes from bound to unbound (and visa-versa). These plots proved to be helpful, illuminating the transient identities of bound atmospheres, marginally bound gas, and low energy ejecta. We adopted the following criterion for ending the calculation: we ceased when all outer shells had positive energy density and the number of intermediate shells with local energy density of changing sign was small – less than a couple of percent of the total mass. An example is shown in Fig. 2, where the apparent bifurcation point is marked. We determined in this case that by the time the code was stopped, the amount of thermal energy remaining in the remnant was insufficient to eject many more mass shells, which is apparent from the diminishing amount of mass ejected with each stellar oscillation. We are confident of this prediction because it has been borne out in all cases where the code was run much longer, and, hence, closer to the point of the remnant’s return to hydrodynamic stability. These plots also showed two

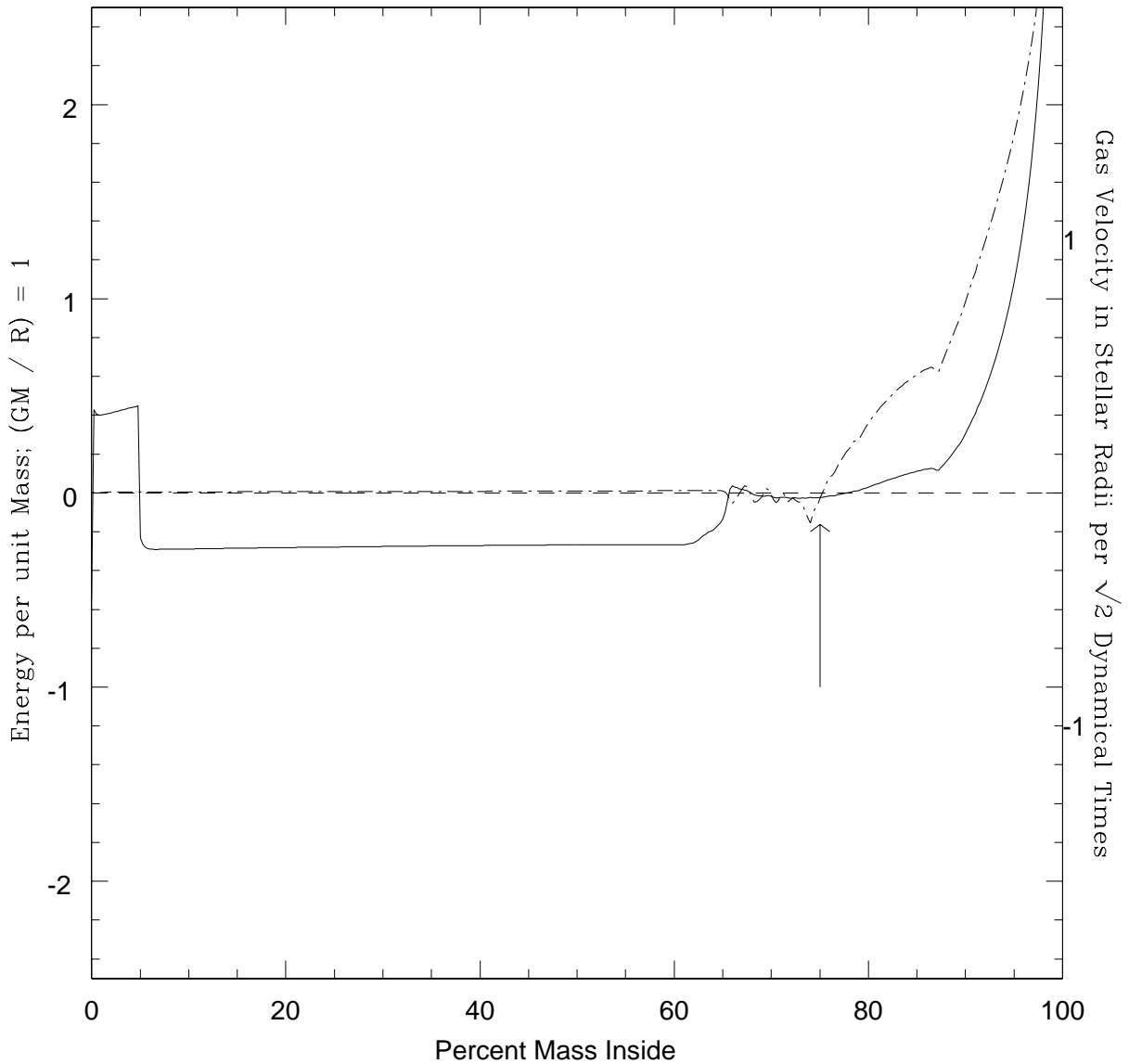


Fig. 1.— The asymptotic local energy density (solid line) for $n = 3$ polytrope (no radiation pressure) and $E_{blast} = E_{bind}$ after the central core has reattained hydrostatic equilibrium, in units for which $(GM/R) = 1$. The dash-dotted line gives the local velocity, in units of stellar radii per $\sqrt{2}$ dynamical times. The dashed line is a reference line for zero energy and velocity.

distinct ways in which shells are ejected: 1) For $0.5 < E_{bind}/E_{blast} < 1.2$ a small number of shells are lost in the initial explosion shock wave; these gain tremendous kinetic energies. The first 8 lines in this plot represent $\sim 4\%$ of the mass; 3-7 % of the mass is lost in this way for this energy range. 2) The rest of the ejecta are expelled by the star as the remnant damps.

Given our algorithm for the determination of mass loss in an explosion, we next investigated the extreme limits: total disruption explosions and failed explosions (no ejected mass). Total disruptions were relatively easy to recognize when all grid zones acquired positive energy in the first pass of the shock wave from the explosion. The minimum blast energy to disrupt was more difficult to determine because the remnants, especially those with higher values of s_1 , have very long relaxation time scales, with their viscous-relaxation time scale being tied to their dynamical time scale since the artificial viscosity dissipates only while the star is contracting. However, it was clear from the results that total disruption happens abruptly, with every star studied going from 50% mass loss to total disruption with only a small addition of explosion energy. We were able to pin down the width of the transition from remnant to total disruption as function of explosion energy to $\sim 5\%$ in the star’s binding energy.

The failed explosion regime was computationally easier to study. Failed explosions produced no outgoing shells with positive energy. The results can be understood in terms of the speed of the shock as it proceeded through the star. Strong shocks slowed as they plowed through the dense core of the star, then accelerated when they reached the diffuse outer regions of the polytropes. In failed explosions the shock velocity fell below the sound speed in the middle region and/or failed to accelerate up to the local escape speed in the outer region. A plot of the process is included in Fig. 3. In the figure, we plot $v_{shock}/\sqrt{v_{esc}^2 + c_{snd}^2}$ – where v_{esc} is the escape velocity for the initial star and c_{snd} is the local sound speed – illustrating the falling shock Mach number in the core and the reacceleration to velocities allowing escape by the outer density gradient.

4.3. Explosions without Radiation Pressure

For the first round of explosions, we used EOS M (no radiation pressure). The advantages to this part of the calculation were that it was slightly more computationally speedy and, more importantly, that the results obtained here can be scaled much more freely to various stellar masses and radii. As we noted before, this is because setting s_c , the radiation-to-matter pressure ratio at the center, essentially amounts to constraining the relationship between stellar mass and radius. For these calculations, the only variables were E_{blast}/E_{bind}

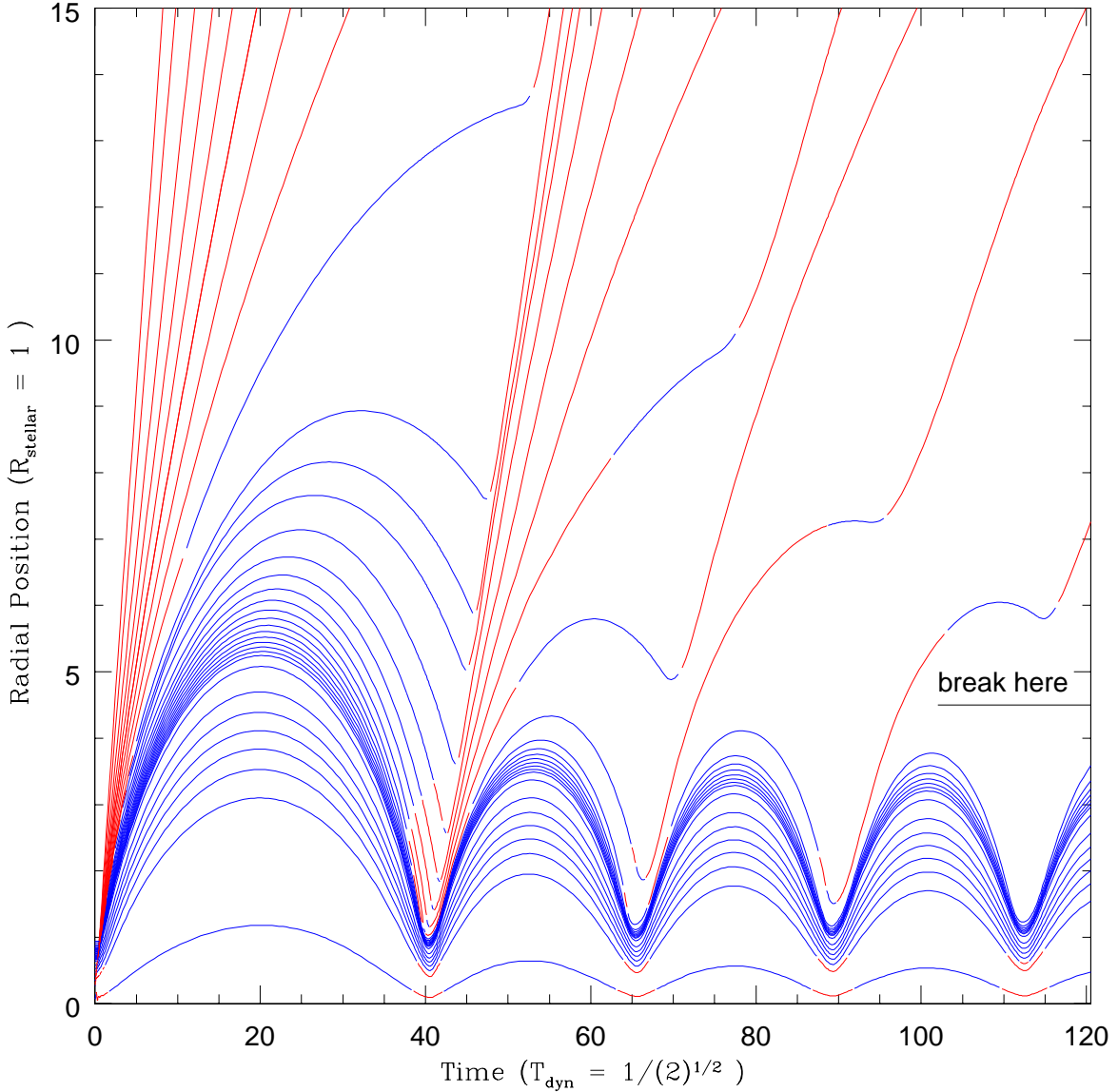


Fig. 2.— A typical graph of the motion of grid zones in time for an exploding star, in this case a polytrope of index $n = 3/2$ with an explosion energy of 90% of the star’s binding energy and with $s_c = 0.5$. Each line tracks a representative mass shell. The Lagrangian mass intervals vary: lines in the ejected region and outer parts of the remnant – which represent escaping mass (large radii) and uppermost parts of the cooling, bouncing remnant (the blue lines) – are intervals of 0.5 – 1% of the total mass. In the inner part of the remnant, each line represents approximately 10% of the total mass. Where lines are red, the local energy density is positive; where blue, negative. The bifurcation point separating the remnant from the ejecta is marked. Radial distances are given in units of the initial stellar radius; times are given in units equal to $\sqrt{2}$ dynamical times.

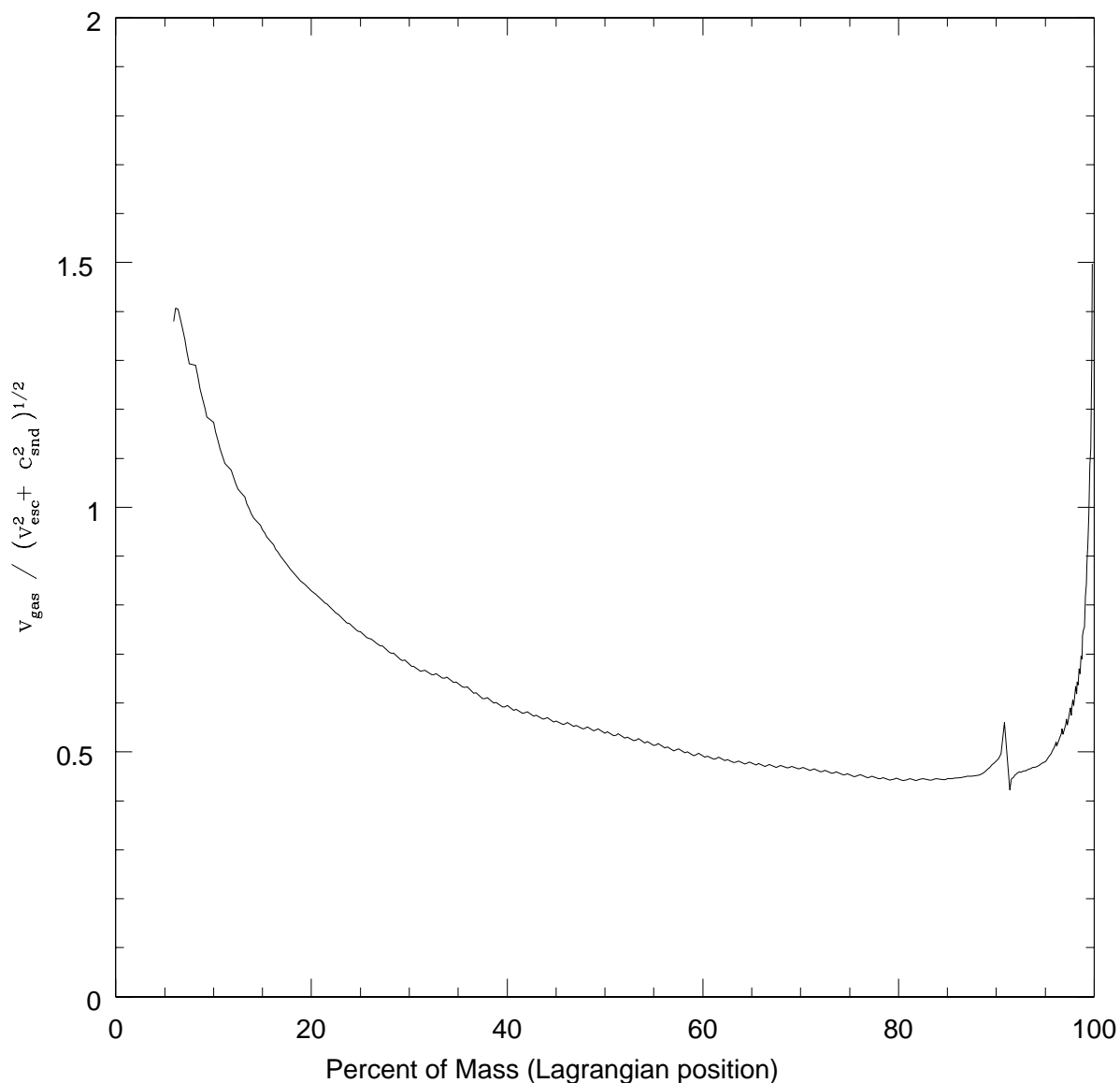


Fig. 3.— A plot of the $v_{gas}/\sqrt{v_{esc}^2 + c_{snd}^2}$ in this case for a star with $n = 1.5$, $s_c = 0.1$, and an explosion energy equal to 15% of the star's binding energy. The choppiness in the plot is due to non-physical effects in the determination of the exact location of the shock. Note the deceleration through the bulk of the star, with only the very outermost shells reaching escape velocity as the shock accelerates in the falling density profile near the edge.

and the star’s polytropic index Γ .

We have included two figures summarizing the computational results. In the first, Fig. 4, the explosions are compared with each other, showing the great similarity among the models. In Fig. 5, we have separated each polytrope into its own window to compare its mass loss curve to a couple of versions of the “rule of thumb” suggested by Fryer & Kalogera (2001). The first line, the dash-dotted curve, is the simplest such rule. It represents the mass loss if 100% of the explosion energy were distributed in such a way as to give as many of the outer shells of the star exactly escape velocity, while leaving untouched those parts of the star which remain bound. This is, of course, physically impossible, but it does provide an upper bound on mass loss. The dashed curve represents the actual choice made by Fryer & Kalogera (2001), which essentially splits the explosion energy budget in two, giving 50% to unbind the star directly, and 50% to heat the remnant and to accelerating the ejecta. This somewhat *ad hoc* but more physically reasonable assumption gives results that are much closer to the numerical calculation, but *overestimates mass loss in low energy explosions* and also *overestimates the amount of energy required to completely unbind the star*.

4.4. Explosions with Radiation Pressure

For the second round of explosions, we used the hydrodynamics code with EOS MR (matter and radiation pressure). The parameter space now included three variables: explosion energy, polytropic index, and s_c , the central radiation to matter pressure ratio. Given the similarity of the results of the various polytropes in the radiation-free calculations, we looked at only two different polytropic indices, $n = 3/2$ and $n = 3$. For s_c , we chose four values: 0.1, 0.5, 1.0, and 5.5. The value $s_c = 5.5$ is close to the maximum value, $s \approx 6$, for a star in which no region has a positive local energy density. As s_c grows larger, the effective $\gamma \rightarrow 4/3$ and the total energy of the star tends toward 0 (in units of GM^2/R). The binding energies for our choices of s_c are summarized in table 1.

In contrast to the radiation pressure-free cases, these calculations clearly show a great difference between these two polytropes: the polytropes with $n = 3$ (Fig. 6) have very little variation in mass loss for different radiation pressure fractions, while the polytropes with $n = 3/2$ (Fig. 7) shows quite a marked variation. Selected testing for $n = 2$ and 4 polytropes suggests that the amount of variation of mass loss with respect to the s_c , radiation pressure fraction parameter, is inversely correlated to polytropic index; *i.e.*, those stars with higher n (and, hence, greater central concentration) have mass loss curves that are less sensitive to radiation fraction, while those with lower n are more sensitive.

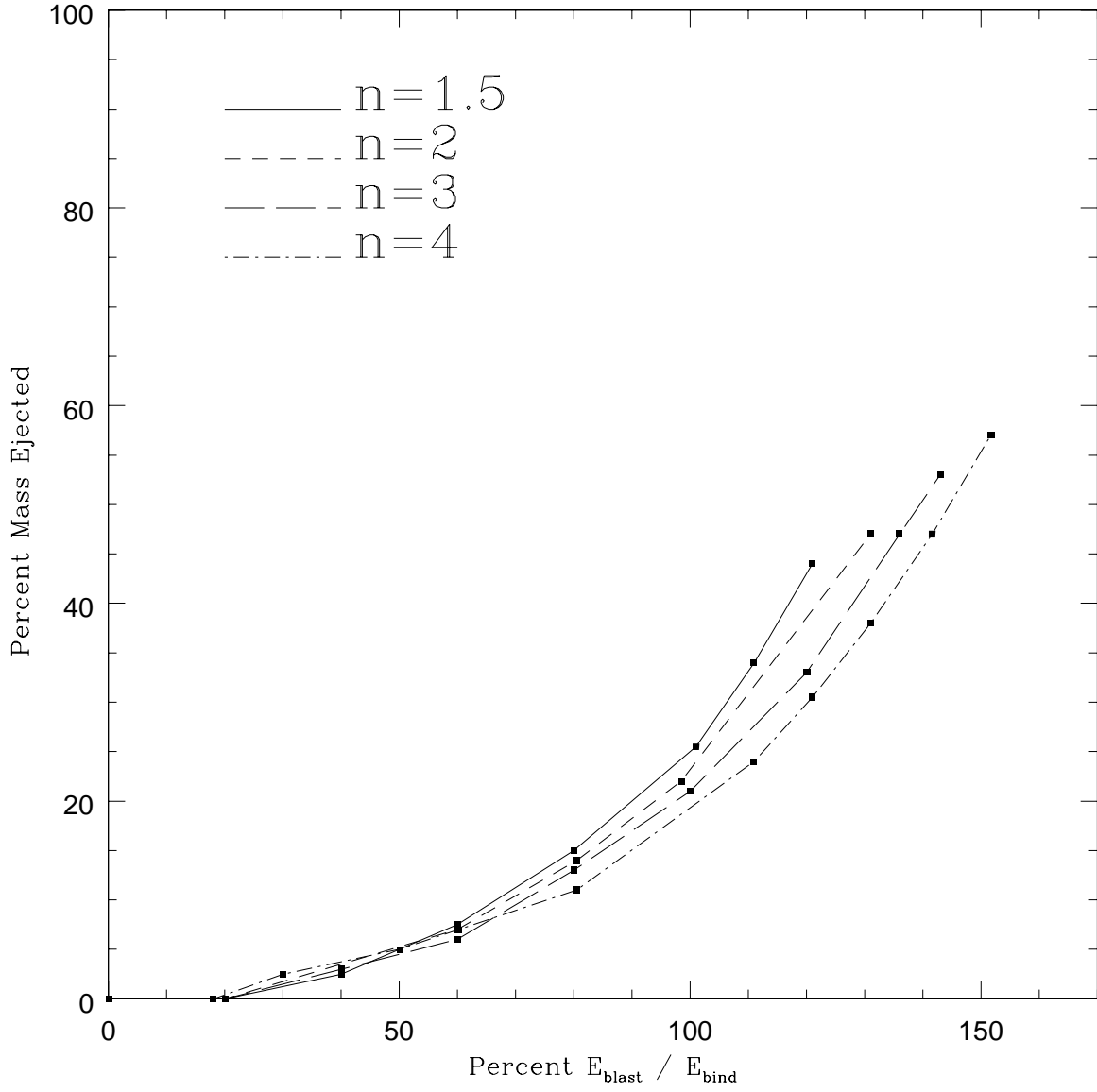


Fig. 4.— This figure summarizes the mass loss percentages resulting from explosions in polytropes of four different indices.

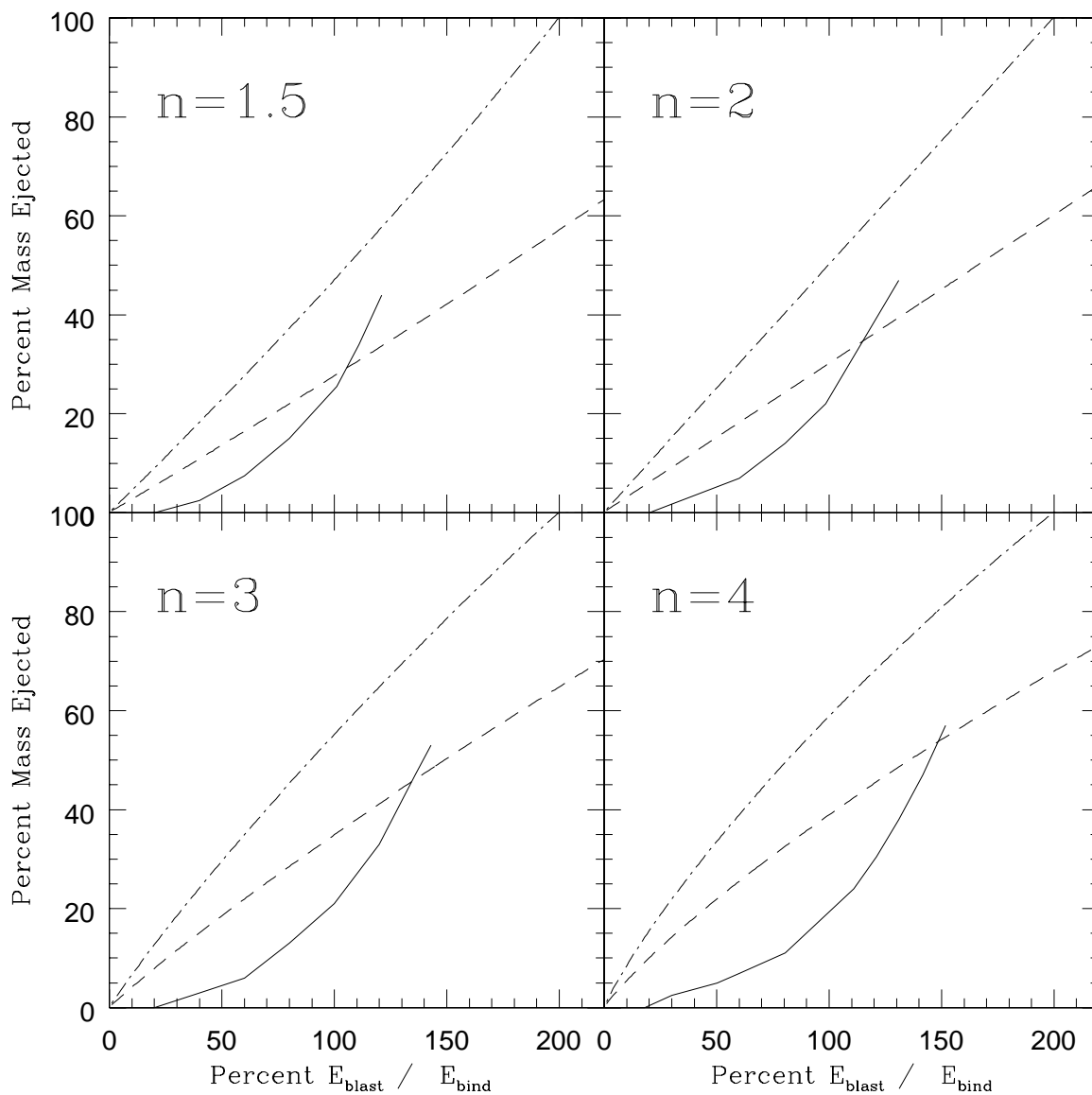


Fig. 5.— Mass loss curves are compared with two simple assumptions relating explosion energy and mass loss. The steeper, dashed curve represents the most efficient possible application of the explosion energy to mass loss. The second, dash-dotted curve represents the more physically reasonable assumption that 50% of the energy goes into unbinding part of the star, and 50% goes into both heating the remaining star and to net kinetic energy for the ejecta.

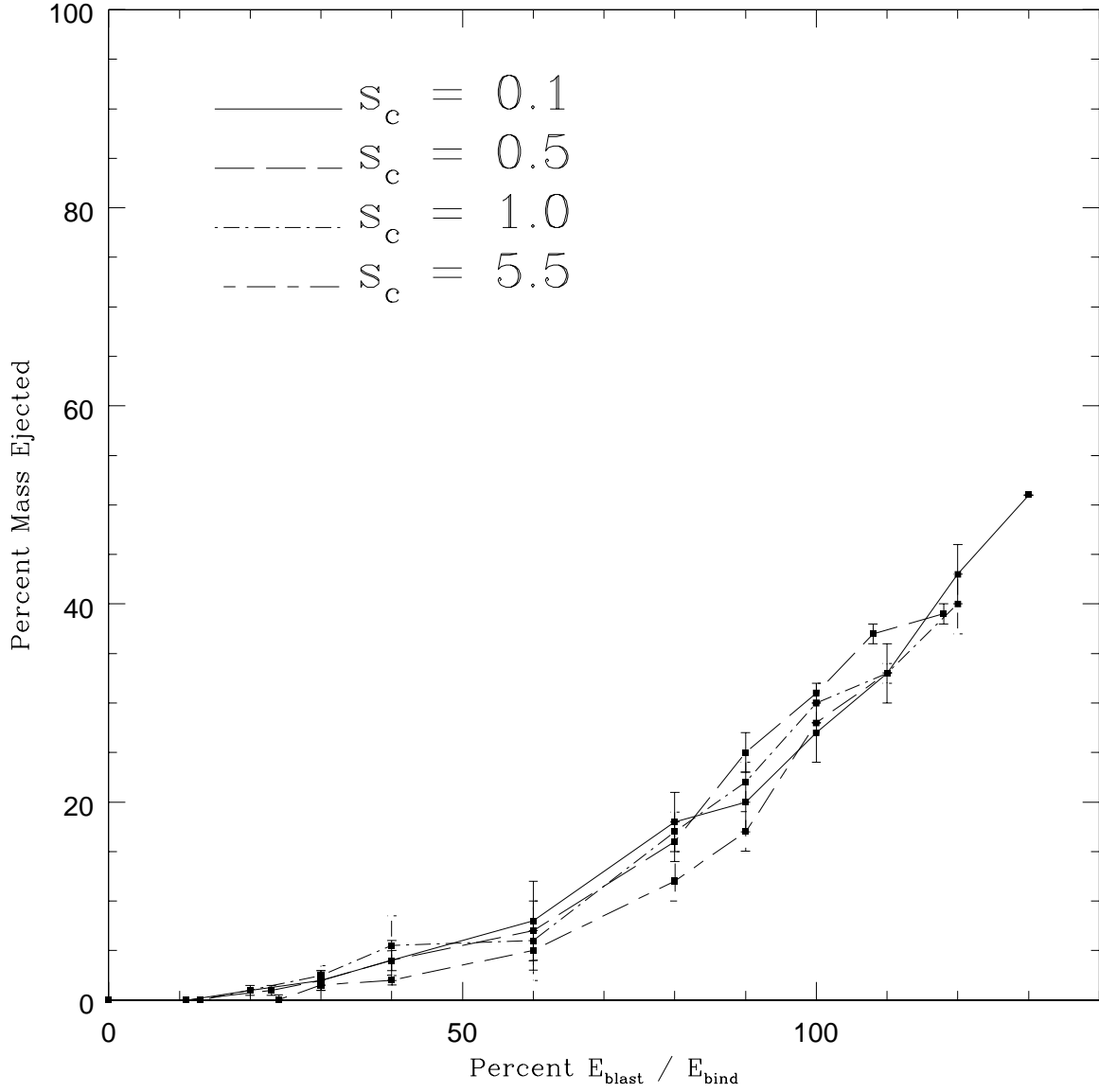


Fig. 6.— This figure summarizes the mass loss percentages for explosions in $n=3$ polytropes for various values of the parameter s_c , the central matter-to-radiation pressure ratio in the progenitor.

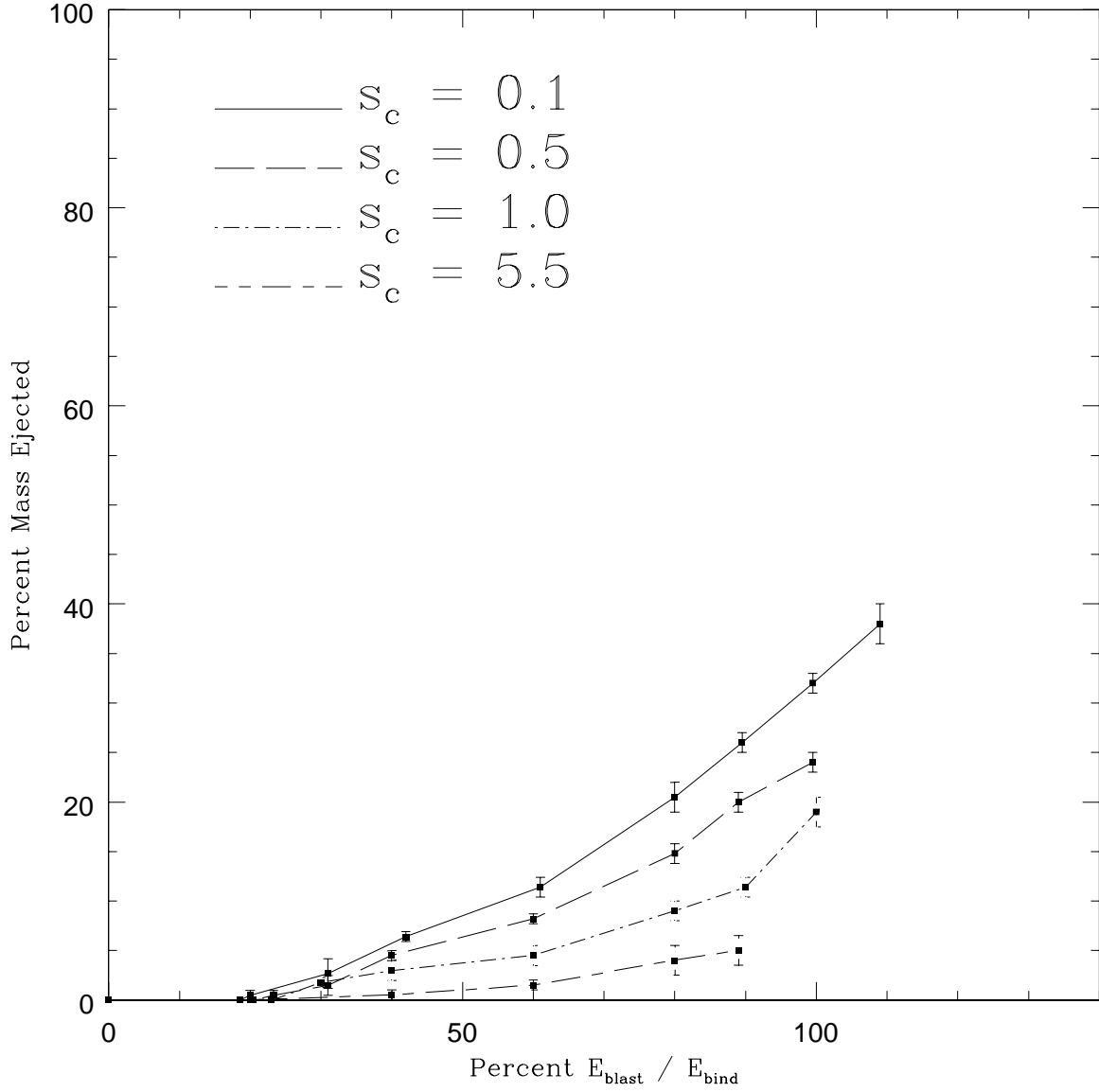


Fig. 7.— This figure summarizes the mass loss percentages for explosions in $n=1.5$ polytropes at various values of the parameter s_c , the central matter-to-radiation pressure ratio in the progenitor.

Table 1: Binding energies for various choices of s parameter. For polytropes, $E_{bind}(s_c = 0) = -(3/2)/(5 - n) \times GM^2/R$.

-	$n = 3/2$	$n=3$
s_c	$E_{bind}/E_{bind}(s_c = 0)$	$E_{bind}/E_{bind}(s_c = 0)$
0	1	1
0.1	0.993	0.994
0.5	0.9322	0.9386
1.0	0.8194	0.8263
5.5	0.3226	0.3204

The uniformity in the shapes of the mass-loss curves found here allows them to be described accurately by a fitting formula. The form that best fits the data is

$$M_{lost} = A(e_{blast} - e_o)^b \Theta(e_{blast} - e_f) \tag{1}$$

where M_{lost} is the mass lost measured as a percent of total stellar mass, e_{blast} (e_o , e_f) is blast energy (minimum blast energy to cause mass loss, maximum blast energy to leave a bound core) measured as a percent of binding energy (*i.e.* $e_{blast} = 100 \times E_{blast}/E_{bind}$, etc.) , and A and b are fitting parameters. A sample comparison between the fits and the numerical data is shown graphically in Fig. 8; the parameters describing each explosion’s fit are contained in table 2.

5. Conclusion

Here, we have confined ourselves to a rather idealized and simplified problem, partially disruptive explosions of progenitors whose density profiles are solutions to the Lane-Emden equation, but with varying ratios of radiation to matter pressure. In this way, we have been able to survey models in a well-defined parameter space fairly extensively. Specifically, we have determined the fraction of the original stellar mass ejected as a function of explosion energy in polytropes of index $n = 1.5, 2, 3$, and 4 in calculations without radiation pressure; we also explored the mass loss fractions for $n = 1.5$ and 3 polytropes with a variety of radiation to matter pressure ratios. Our results suggest that the mass loss of centrally concentrated, large n models is relatively insensitive to radiation pressure, whereas the mass loss of relatively diffuse, low n polytropes is suppressed by increasing central radiation pressure. We have provided a simple, parametrized formula for the fractional mass loss as a function

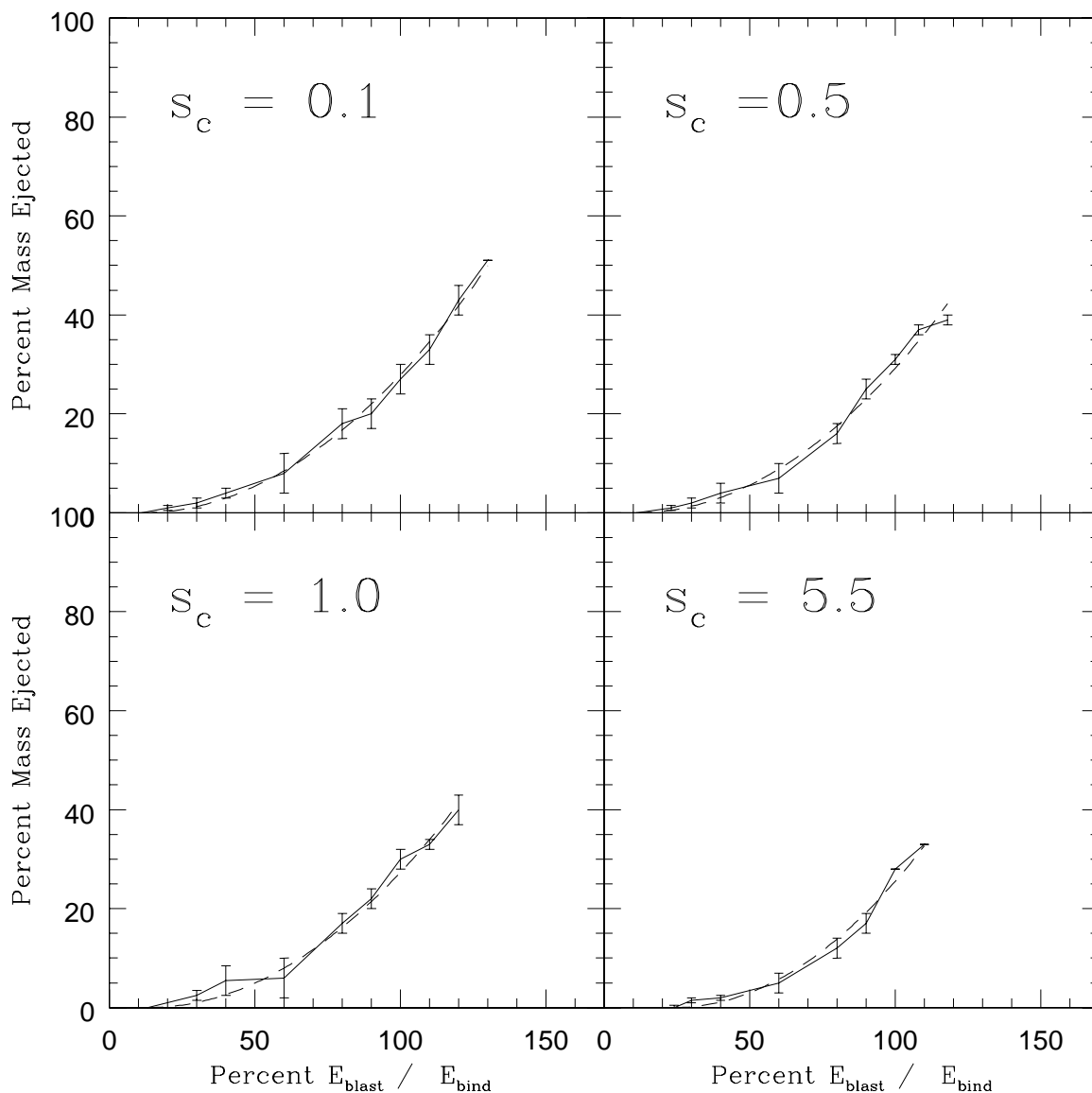


Fig. 8.— This figure shows the comparison between the numerical data (solid line) and the curve fit to that data, in this case for $n = 3$ supernovae at various values of s_c , the parameter describing the central matter-to-radiation pressure ratio. The other fits are similarly successful. The error bars shown represent an estimate of the uncertainty in our determination of the percent mass ejected.

Table 2: Summary of fitting parameters for various explosion scenarios. $e_o = 100 \times E_o/E_{bind}$, $e_f = 100 \times E_f/E_{bind}$

n	s_c	$A(\times 10^{-3})$	b	e_o	e_f
3/2	0	4.17	2	20	121
“	0.1	43.7	1.5	18	109
“	0.5	34.0	1.5	20	99.5
“	1.0	24.3	1.5	23	100
“	5.5	12.8	1.5	20	90
2	0	3.72	2	20	131
3	0	3.15	2	20	132
“	0.1	3.52	2	11	130
“	0.5	3.69	2	11	118
“	1.0	3.61	2	13	120
“	5.5	4.42	2	13	110
4	0	3.05	2	18	152

of explosion energy for a range of values of n and the ratio of radiation to matter pressure.

One striking feature of all the models we tested was that the mass loss fraction as a function of explosion energy appears to be discontinuous at around 50 % mass loss, with a small (few %) difference in explosion energy separating stars which lose half their mass from totally disrupted stars. Because our simulations did not include formation of a compact remnant at the center, this result cannot be taken as a concrete demonstration that the observation of a black hole of mass M demands a progenitor whose mass was less than about twice as large.

However, the abrupt transition between moderate (i.e. $\lesssim 50\%$) and almost total disruption found here for wide classes of initial models is also seen in modelling of explosions in sets of specific progenitors (e.g. Woosley & Weaver (1995), Table 3; MacFadyen, Woosley & Heger (2001), Table 1). Thus, we conjecture that even when a compact central remnant is included, the results divide into two separate cases depending on whether the explosion energy is above or below, approximately, the critical value found here for complete disruption. For explosion energies below this critical value, there is a sharp transition between modest (i.e. $\lesssim 50\%$) mass loss and total disruption apart from the compact remnant. For explosion energies above the cutoff, either a black hole or neutron star may form. However, in this case, we expect much smaller fallback masses, generally only a few tenths of M_\odot or

less, primarily caused by reverse shock propagation through the core, and the consequent deceleration of a small amount of outgoing matter (e.g. Woosley (1988); Chevalier (1989)).

In systems with very energetic explosions and little mass fallback we expect little mass contamination of the atmosphere of the binary companion. The outgoing regions of the progenitor intercepted by the companion are not captured; indeed the outer layers of the companion are stripped and ablated by the ejecta. On the other hand, when the explosion is weak and substantial mass fallback occurs, progenitor material may fall back onto the companion, polluting its atmosphere. In the latter cases, we would then infer that a remnant of mass M was most likely derived from a progenitor with mass less than $\simeq 2M$. Thus, in systems like Nova Scorpii that show evidence for black hole formation in a supernova (e.g. Israelian et al. (1999)), we conjecture that mass of the pre-explosion star was, in fact, less than twice the present mass inferred for the black hole remnant (which also has accreted matter since forming, presumably). This may have implications for the dynamics of such systems (e.g. Mirabel et al. (2002)). We caution, though, that our results may be altered somewhat in more refined models. Further studies are underway to include a compact central remnant, density jumps (expected as a consequence of compositional inhomogeneity), rotation and explosion asymmetries. These new calculations will continue, in the same spirit as those reported here, to employ the simplest explosion models needed to reveal the underlying physical consequences of the various refinements, and to allow a survey the explosion hydrodynamics of a large range of explosion models.

This research was supported in part by NASA-ATP grant NAG5-8356. M.W. is supported by an NSF Graduate Fellowship. I.W. acknowledges the hospitality of KITP, which is supported by NSF grant PHY99-07949, where part of this research was carried out.

A. Appendix A: Difference Equations

The Lax-Wendroff difference equations for the equations of hydrodynamics in one dimension with spherical symmetry are as follows. Note that the pressure in the equation for advancing energy must be solved for using the equation of state to make this set of difference equations explicit rather than implicit. In the difference equations, n represents time steps, while j represents spatial steps. The equations are non-dimensionalized simply, with each variable scaled to order unity for the initial conditions in all calculations we have done. The one remaining constant, ρ_o , with units of density, sets the overall scale of the system studied. The variable R records the position of each shell. Comparing each shell's current position, R , with r , a static, reference grid, allows the gas's local density to be calculated.

The remaining variables are interdependent. The equation for moving grid zones is:

$$\frac{R_j^{n+1} - R_j^n}{\Delta t} = u_j^{n+1}. \quad (\text{A1})$$

The conservation of momentum equation is:

$$\frac{u_j^{n+1} - u_j^n}{\Delta t} = -\frac{1}{\rho_o} \frac{(\delta p)_j^n}{\Delta r} \left(\frac{R_j^n}{r_j} \right)^2. \quad (\text{A2})$$

The conservation of mass equation is:

$$\rho_{j+1/2}^{n+1} = \rho_o \frac{(r_{j+1})^3 - (r_j)^3}{(R_{j+1}^{n+1})^3 - (R_j^{n+1})^3}. \quad (\text{A3})$$

The First Law of Thermodynamics is:

$$U_{j+1/2}^{n+1} = U_{j+1/2}^n - \left(\frac{p_{j+1/2}^{n+1} + p_{j+1/2}^n}{2} \right) \times \left(\frac{1}{\rho_{j+1/2}^{n+1}} - \frac{1}{\rho_{j+1/2}^n} \right). \quad (\text{A4})$$

Where U = internal energy / mass. The acceleration of the innermost shell is determined by treating its volume as filled with a gas of uniform pressure so that the shell's equation of motion is:

$$m_{inner} \frac{\partial v}{\partial t} = 4\pi(p_{inner} - p_{outer}) \Rightarrow \quad (\text{A5})$$

$$u_0^{n+1} = u_0^n + 4\pi\Delta t(p_{inner} - p_{outer}). \quad (\text{A6})$$

The pressure within the inner sphere varies adiabatically as the shell moves, *i.e.*,

$$p_{inner}(t) = p_o \left(\frac{V_o}{V(t)} \right)^\gamma. \quad (\text{A7})$$

These equations are completed by some equation of state,

$$p_{j+1/2}^{n+1} = f(U_{j+1/2}^{n+1}, \rho_{j+1/2}^{n+1}). \quad (\text{A8})$$

If this equation of state can be algebraically solved, the full set of equations is explicit; if it cannot be solved, then an implicit step and numerical root-finding procedure is required to advance the grid. The advancement of the grid proceeds as follows. 1) Using the conservation of momentum, the new gas velocities are set throughout the system. 2) Boundary conditions

are applied. 3) The shell position, R , is advanced according to the new gas velocities. 4) R is then used to set the density throughout the system. 5) Two possibilities: if the equation of state is explicitly soluble, then the internal energy of the gas is determined. If not, then the pressure and energy equations must be stated in terms of the temperature and then solved, together with the First Law, numerically – three equations for three variables, p , U , and T . The above prescription must be modified slightly to accommodate shock fitting. To this end, we introduce an artificial viscous pressure, q , given by the differenced form,

$$q_{j+1/2}^n = \begin{cases} \frac{2a^2[(\delta u)_{j+1/2}^n]^2}{1/\rho_{j+1/2}^n + 1/\rho_{j+1/2}^{n-1}} & \text{if } (\delta u)_{j+1/2}^n < 0 \\ 0 & \text{if } (\delta u)_{j+1/2}^n \geq 0 \end{cases} \quad (\text{A9})$$

Note the parameter, a , which controls how widely the viscous pressure spreads the shock. Optimal values are $1.5 < a < 2.0$, which spread the shock over 3-10 zones. This artificial viscous pressure is added to the regular gas pressure in the above equations as follows: In the conservation of momentum equation,

$$(\delta p)_j^n \rightarrow (\delta p)_j^n + (\delta q)_j^n \quad (\text{A10})$$

and in the energy conservation equation,

$$\frac{p_{j+1/2}^{n+1} + p_{j+1/2}^n}{2} \rightarrow \frac{p_{j+1/2}^{n+1} + p_{j+1/2}^n}{2} + q_{j+1/2}^{n+1}. \quad (\text{A11})$$

When advancing the grid with artificial viscous pressure, the artificial viscosity term, q , is advanced before the energy equation, step 5 in the previous description.

In the simulations we ran, we used two equations of state. One without radiation pressure,

$$\rho U = nkT, \quad (\text{A12})$$

one with radiation pressure,

$$\rho U = nkT + aT^4. \quad (\text{A13})$$

The first is explicitly soluble; the second is not. Non-dimensionalizing the first formula is simple; non-dimensionalizing the second requires us to introduce a new parameter, s , which describes the relative sizes of the radiation and matter pressure. We define s as

$$s_c = \frac{p_{rad}}{p_{matter}} = \frac{ma}{3k} \left(\frac{T^3}{\rho} \right)_{center}. \quad (\text{A14})$$

In terms of s , the non-dimensionalized forms of the expressions for internal energy and pressure become,

$$\tilde{p} = \frac{\tilde{\rho}\tilde{T}}{(1+s)} + \frac{\tilde{T}^4}{(1+1/s)} \quad (\text{A15})$$

$$\tilde{\rho}\tilde{U} = \frac{\tilde{\rho}\tilde{T}}{(\gamma - 1)(1 + s)} + 3\frac{\tilde{T}^4}{(1 + 1/s)} \quad (\text{A16})$$

where the tildes indicate dimensionless quantities: $\tilde{p} = p/p_{center}$, $\tilde{T} = T/T_{center}$, etc. These equations are solved together with the First Law to determine p and U for each time step.

For all calculations done after the code was tested, we also included a Newtonian Gravitation force per unit mass via

$$F_{grav} = -\frac{GM(R)}{R^2}, \quad (\text{A17})$$

or in difference form,

$$F_j^n = -\frac{G\rho_o \frac{4\pi}{3}(r_j^n)^3}{(R_j^n)^2}. \quad (\text{A18})$$

This force was added to the conservation of momentum equation, the equation used to set gas velocities. Finally, the code self-checks by calculating total energy and momentum to ensure that these are conserved. For energy, the sum of the local energy in each zone is calculated first *via*

$$E_{kinetic} + E_{therm} = \sum_{i \in \text{zones}} \left(\frac{1}{2}u_i^2 + U_i \right) \Delta M_i. \quad (\text{A19})$$

The gravitational potential energy is then calculated via

$$E_{grav} = - \sum_{i \in \text{zones}} \frac{GM_{enclosed}}{R_i} \Delta M_i. \quad (\text{A20})$$

and the two energies are added and recorded as the current total energy in the system. Conservation of momentum is also checked though a simple summation:

$$P_{tot} = \sum_{i \in \text{zones}} u_{zone} \Delta M_i. \quad (\text{A21})$$

Finally, the algebraic equation used to determine the total local energy per unit mass of each zone – the quantity used to determine if a zone was bound or unbound – was

$$\begin{aligned} \frac{E_{zone=j}^{tot}}{\Delta M_j} &= \frac{E_j^{therm} + E_j^{kinetic} + E_j^{potential}}{\Delta M_j} \\ &= \frac{1}{2}u_j^2 + U_j - \frac{1}{2} \sum_{i=1}^{i \leq j} F_i^{grav} \Delta R_i, \end{aligned} \quad (\text{A22})$$

where $\Delta R_i = R_i - R_{i-1}$.

B. Appendix B: Sedov Solution

For the analytic solution to the Sedov problem, we rederived the solution given in Landau and Lifshitz's *Fluid Mechanics*, thereby finding the correction to the often remarked upon error (in an exponent) in that book's solution. The independent variables are t and r . In the similarity solution, lengths are measured with respect to the shock radius so that $r = R_s(t)$ corresponds to $\xi = 1$, where ξ is the similarity variable

$$\xi = r \left(\frac{\rho_o}{E_o t^2} \right)^{1/5}.$$

The preshock density is ρ_o and the explosion energy is E_o . For the following equations, the fluid velocity (in the frame in which the center of the remnant is at rest) is V and the local adiabatic speed of sound is c_s .

Define the dimensionless density, fluid velocity and sound speed squared

$$G(\xi) = \frac{\rho}{\rho_o}, \quad U(\xi) = \frac{5t}{2r}V, \quad Z(\xi) = \frac{25t^2}{4r^2}c_s^2.$$

Directly behind the shock,

$$G(1) = \frac{\gamma + 1}{\gamma - 1}, \quad U(1) = \frac{2}{\gamma + 1}, \quad Z(1) = \frac{2\gamma(\gamma - 1)}{(\gamma + 1)^2}.$$

A solution is

$$\begin{aligned} \xi^5 &= \left(\frac{\gamma + 1}{2}U \right)^{-2} \left(\frac{\gamma + 1}{7 - \gamma}[5 - (3\gamma - 1)U] \right)^{\nu_1} \times \\ &\quad \left(\frac{\gamma + 1}{\gamma - 1}(\gamma U - 1) \right)^{\nu_2} \\ G &= \frac{\gamma + 1}{\gamma - 1} \left(\frac{\gamma + 1}{\gamma - 1}(\gamma U - 1) \right)^{\nu_3} \times \\ &\quad \left(\frac{\gamma + 1}{7 - \gamma}[5 - (3\gamma - 1)U] \right)^{\nu_4} \left(\frac{\gamma + 1}{\gamma - 1}(1 - U) \right)^{\nu_5} \\ Z &= \frac{\gamma(\gamma - 1)U^2(1 - U)}{2} \frac{1}{\gamma U - 1} \end{aligned}$$

where

$$\begin{aligned} \nu_1 &= -\frac{(13\gamma^2 - 7\gamma + 12)}{(2\gamma + 1)(3\gamma - 1)} & \nu_2 &= \frac{5(\gamma - 1)}{2\gamma + 1} \\ \nu_3 &= \frac{3}{2\gamma + 1} & \nu_4 &= -\frac{\nu_1}{2 - \gamma} & \nu_5 &= -\frac{2}{2 - \gamma} \end{aligned}$$

REFERENCES

- Chevalier, R. A. 1989, Ap. J., 346, 847.
- Fryer, C. L. & Kalogera, V. 2001, ApJ, 554,548
- Israelian, G., Rebolo, R., & Basri, G., 1999, Nature, 401, 142
- Landau, L. D., and Lifshitz, E. M. 1987, Fluid Mechanics, Pergamon Press: Oxford
- MacFadyen, A. I., Woosley, S. E., & Heger, A., 1999, ApJ, 524, 262
- MacFadyen, A. I., Woosley, S. E. and Heger, A. 2001, Ap. J., 550, 410.
- Mirabel, I. F., Mignani, R., Rodrigues, I., Combi, J. A., Rodríguez, & L. F., Guglielmetti, F. 2002, A&A, 395, 595
- Orosz, J. & Bailyn, C. 1997, ApJ, 477, 876
- Richtmyer, R. & Morten, K. W. 1967, Difference Methods For Initial-Value Problems, John Wiley & Sons: New York
- Shahbaz, T, van der Hooft, F, Casares, J, Charles, P. A., & van Paradijs, J. 1999, MNRAS, 306, 89
- Woosley, S. E. 1988, Ap. J., 330, 281.
- Woosley, S. E. and Weaver. T. A. 1995, Ap. J. Supp., 101, 181.